*Progress In Electromagnetics Research Letters, Vol. 33, 151–166, 2012*

# DESIGN AND OPTIMIZATION OF HIGH SENSITIVITY PHOTONIC INTERFEROMETRIC BIOSENSORS ON POLYMERIC WAVEGUIDES

**G. Calò*, A. Farinola, and V. Petruzzelli**

Dipartimento di Elettrotecnica ed Elettronica, Politecnico di Bari, Via Re David n. 200, Bari 70125, Italy

**Abstract**—The design criteria of integrated optical biosensors based on the Mach-Zehnder Interferometer and on the Michelson Interferometer are proposed. Sensitive performance has been evaluated for different optical polymeric waveguiding structures such as channel, inverted-rib and strip waveguides. For all the configurations of the examined optical waveguiding interferometric biosensors maximum linearity and sensitivity have been obtained. In particular, the achieved sensitivity, expressed as the ratio between the normalized output power and the protein concentration, is about equal to $1.6\,(\mathrm{g/ml})^{-1}$ which, for a maximum variation of the output power equal to 100 mW, leads to a non-normalized sensitivity equal to 160 mW/(g/ml).

## 1. INTRODUCTION

In recent years there has been a growing interest in the development of biosensors that allow efficient conversion of chemical or biological reactions into a measurable signal, useful to the health, environmental pollution, and medical diagnostics. In particular, the optical sensors offer many advantages with respect to other technologies thanks to their high sensitivity, their immunity to electromagnetic interference, their excellent compactness and robustness and the high compatibility with optical fibers generally used for the long distance transmission of the optical signals [1, 2].

In optical biosensing, different interaction mechanisms can be exploited to convert the variation of the concentration of the biological agent into an optical signal. For example, evanescent field sensors, based on waveguide or Photonic Crystal Fiber (PFC) configurations,

---

*Received 13 May 2012, Accepted 1 July 2012, Scheduled 25 July 2012*

* Corresponding author: Giovanna Calò (g.calo@deemail.poliba.it).

have been proposed to detect hydrocarbons or methadone in polluted water [3–5]. In these cases, the sensing principle is based on the concentration-dependent interaction between the modal evanescent field and the sensitive layer (polymer layer) surrounding the waveguiding structures. In photonic crystals and in plasmonic sensors, the presence of the biological agent (e.g., $H_2$ in the human breath or human chorigonadotropin (hGC)) or, more generally speaking, the variation of the quantity under investigation causes, for example, the shift of the resonance condition and therefore the variation of the optical response of the system [6–11].

In this paper, we focus on integrated optical biosensors based on polymeric waveguides assembled into Mach-Zehnder (MZI) and Michelson (MI) interferometric configurations. Interferometric biosensors exploit the refractive index change induced by the biological agent, and the consequent change in the interference condition, to achieve high sensitivity values combined with simple design rules and low manufacturing cost, thanks to the use of polymers [12–23].

Polymeric materials are indeed particularly promising for the realization of waveguides thanks to the possibility of tailoring their optical properties and to their processing ease [24]. In this work, we focus on two particular polymers, i.e., the polymethylmethacrylate (PMMA) and the epoxy resin SU-8. The PMMA is a transparent material having good properties of hardness, rigidity and a high UV stability [25, 26]. The SU-8 is a common negative photoresist combining advantageous properties such as flexibility, adhesion and chemical resistance. It combines the excellent mechanical properties, with excellent adhesion and electrical insulation as well as a strong resistance to chemical agents and temperature. The SU-8 photoresist and the PMMA are among the most biocompatible polymers and this, together with their physical and optical properties, make them suitable for biological and chemical sensing applications [25, 27].

This paper focuses on the design and the optimization of photonic biosensors and, through the electromagnetic analysis, it aims at the definition of a methodology allowing to simply, but yet effectively, design interferometric biosensors with different waveguiding structures.

Here, different waveguiding structures are analyzed such as channel, strip, and inverted-rib waveguides, made of an SU-8 core laying on a PMMA or $SiO_2$ substrate and covered by PMMA cladding. Moreover, the performances obtained by two interferometric configurations, i.e., Mach-Zehnder and Michelson, used as biosensors in the detection of the protein concentration in solution, are compared and the optimal design criteria are outlined. In particular, the geometric parameters of the three different waveguides have been optimized in order to assure the single-mode propagation and the maximum interaction between the guided optical mode and the biological sample. In this way, higher sensitivity to protein concentration change can be achieved. Subsequently, a design method of the geometric parameters of the interferometric biosensors is reported, focusing, in particular, on the length of the sensitive zone where the biological solution replaces the PMMA cover layer.

## 2. DESIGN OF THE OPTICAL WAVEGUIDES

Figure 1 shows the three different configurations of the analyzed waveguides: (a) channel waveguide, (b) strip waveguide and (c) inverted-rib waveguide. The waveguides are made of an SU-8 core placed on a substrate of PMMA, for the channel and the rib-inverted waveguides, and on an $SiO_2$ substrate for the strip waveguide. In the sensitive zone, the PMMA cladding is partially removed thus allowing the infiltration of a solution, here referred to as biolayer, with variable concentration of biological agent (i.e., protein in solution). Table 1 shows the refractive index values for the three analyzed waveguides at the operation wavelength $\lambda = 0.633\,\mu\text{m}$.

The thickness $d$ and the width $w$ of the waveguides have been suitably chosen in order to ensure, in addition to the single mode behavior, the best response within the range of variability of the

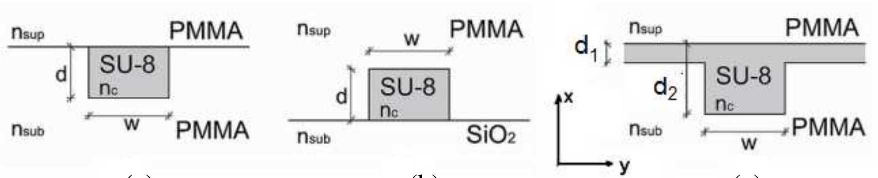

(a) (b) (c)

**Figure 1.** Cross sections of: (a) channel, (b) strip, (c) inverted-rib waveguides.

**Table 1.** Refractive indexes of the channel, the inverted-rib, and the strip waveguides at the operating wavelength $\lambda = 0.633\,\mu\text{m}$.

| | Channel | Inverted-rib | Strip |
|---|---|---|---|
| Superstrate refractive index $n_{sup}$ | 1.5 | 1.5 | 1.5 |
| Core refractive index $n_c$ | 1.59 | 1.59 | 1.59 |
| Substrate refractive index $n_{sub}$ | 1.5 | 1.5 | 1.46 |

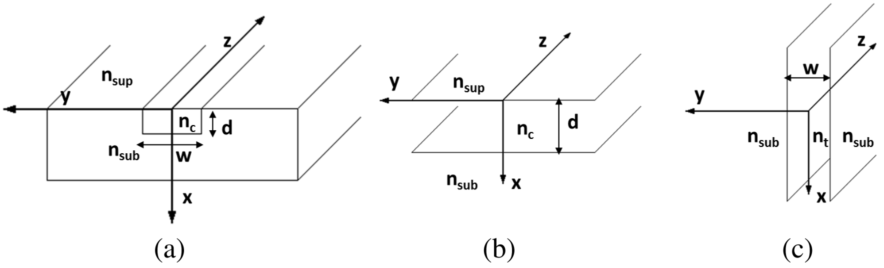

**Figure 2.** Scheme of the REIM applied to the channel waveguide: (a) three-dimensional channel waveguide, (b) slab waveguide stratified along the $x$ direction, (c) slab waveguide stratified along the $y$ direction.

refractive index of the biolayer, $n_{bio}$, from 1.33 to 1.4 [27]. For this purpose, the electromagnetic analysis of the three waveguiding structures was performed by the Refractive Effective Index Method (REIM) [28, 29].

According to the REIM, as schematized in Fig. 2, the three-dimensional waveguide (Fig. 2(a)) is reduced to a two-dimensional one decomposing it, at first, into a slab waveguide stratified along the $x$ direction (Fig. 2(b)) and then into a slab waveguide stratified along the $y$ one (Fig. 2(c)). To analyze the optical propagation of the hybrid $\mathrm{HE}_{11}$ mode we obtained for the $x$-stratified slab waveguide the effective refractive indices of the Transverse Magnetic (TM) mode $n_t$ which are used as core and substrate temporary refractive indices $n_t$ for the slab waveguide stratified along the $y$ direction. According to the REIM, the effective refractive indices $n_{eff}$ of the $\mathrm{HE}_{11}$ mode for the overall three-dimensional waveguide were calculated as the effective refractive indices of the Transverse Electric (TE) mode of the $y$-stratified slab waveguide.

Obviously, the effective refractive indices, $n_t$ and $n_{eff}$, depend on the geometrical and optical parameters of the waveguides and, in particular, they are affected by the variation of the cladding refractive index, i.e., the biolayer, which is induced by the change of the concentration of the biological agent, e.g., proteins in solution. Therefore, the variations of the effective refractive indices, $n_t$ and $n_{eff}$, of the two slab waveguides, stratified along the $x$ and $y$ directions, can be considered as figures of merit useful to quantify the interaction between the propagating optical signal and the biological agent.

In particular, we define the effective refractive index variation

$\Delta n_t^{\mathrm{TM}}$ for the $x$-stratified slab waveguide as:

$$\Delta n_t^{\mathrm{TM}} = n_{t1.33} - n_{t1.44} \tag{1}$$

and the effective refractive index variation $\Delta n_{\mathit{eff}}^{\mathrm{TE}}$ for the $y$-stratified slab waveguide:

$$\Delta n_t^{\mathrm{TE}} = n_{\mathit{eff}1.33} - n_{\mathit{eff}1.44} \tag{2}$$

where $n_{t1.33}$, $n_{\mathit{eff}1.33}$, and $n_{t1.44}$, $n_{n\mathit{eff}1.44}$ are the effective refractive indices of the $x$- and $y$-stratified slab waveguides, respectively, calculated considering the edge values, $n_{bio} = 1.33$ and $n_{bio} = 1.44$, of the range of variability of the biolayer refractive index.

As an example, Fig. 3 shows for the channel waveguide both the variation $\Delta n_t^{\mathrm{TM}}$ and $\Delta n_{\mathit{eff}}^{\mathrm{TE}}$ as a function of the thickness $d$ (Fig. 3(a)) and the width $w$ (Fig. 2(b)) (fixing the thickness $d = 0.4\,\mu\mathrm{m}$), respectively. It can be observed that the maximum variation of $\Delta n_t^{\mathrm{TM}}$ is obtained when $d \cong 0.35\,\mu\mathrm{m}$, whereas $\Delta n_{\mathit{eff}}^{\mathrm{TE}}$ always increases with the width $w$. For the three waveguiding structures we report in Table 2 the optimal geometrical parameters chosen as a good compromise between the single-mode propagation condition and the maximization of both the optical confinement and the $\Delta n_t^{\mathrm{TM}}$ and $\Delta n_{\mathit{eff}}^{\mathrm{TE}}$ values.

The REIM method allows the choice of the dimensions of the optical waveguides according to the criterion of the maximum variation of the effective refractive index. This requirement is propaedeutic to

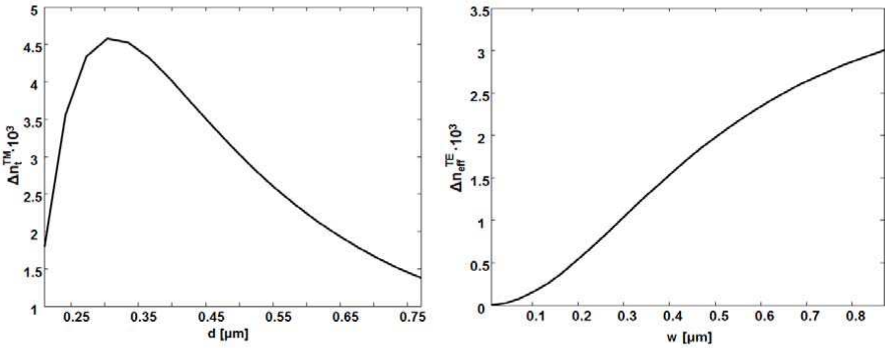

(a) (b)

**Figure 3.** Variation of the effective refractive indices in the case of the channel waveguide calculated by the REIM as a function of the core depth $d$ (a) for the $x$-stratified slab waveguide $\Delta n_t^{\mathrm{TM}} = n_{t1.4} - n_{t1.33}$ and as a function of the core width $w$ (b) for the $y$-stratified slab waveguide $\Delta n_{\mathit{eff}}^{\mathrm{TM}} = n_{\mathit{eff}1.4} - n_{\mathit{eff}1.33}$.

**Table 2.** Geometrical parameters of the three waveguides.

| | **Channel** | **Inverted-rib** | **Strip** |
|---|---|---|---|
| $d$ [μm] | **0.4** | $d_1 = 0.5$, $d_2 = 0.6$ | **0.6** |
| $w$ [μm] | **0.87** | **1.4** | **0.65** |

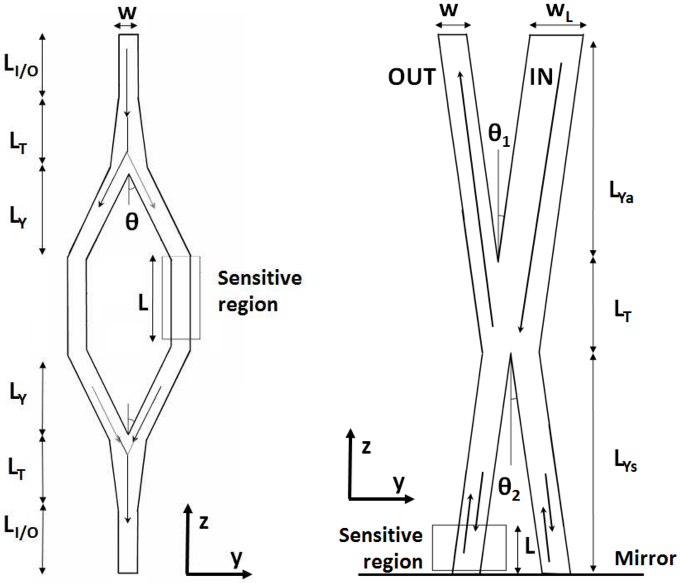

(a) (b)

**Figure 4.** Scheme of (a) the Mach-Zehnder and (b) the Michelson interferometric biosensors.

the achievement of the maximum sensitivity. As will be described in the following, on the basis of the waveguide dimensions given by the REIM, all the other geometrical parameters will be optimized by the FFT-BPM, in order to achieve the best correspondence between the theoretical results and the electromagnetic simulations.

## 3. DESIGN OF THE SENSITIVE REGION

Figure 4 shows the schemes of the examined interferometric Mach-Zehnder (a) and Michelson (b) biosensors. The operation principle of the two interferometric configurations can be briefly described as it follows.

In the MZI version the input signal is equally split into the sensitive and the reference arms. A variation of the concentration of the biological agent causes a change in the refractive index of the biolayer in the sensitive region and a consequent phase shift $\Delta\Phi$ between the optical signals propagating in the two arms. The two optical signals recombine at the output port so that the output power depends on the phase shift experienced by the two propagating signals according to the biolayer refractive index.

Conversely, the MI version, shown in Fig. 4(b), is an X-shaped interferometer which exploits an adiabatic asymmetric $Y$-junction, a taper, a symmetric $Y$-junction, and a mirror. The input signal propagates in the forward direction, toward the taper and the symmetric $Y$-junction, where it is equally split into the two waveguiding arms. At the mirror interface, the optical signals propagating in the two arms are reflected back and, after recombining in the taper, they are again split in the adiabatic asymmetric $Y$-junction. Thanks to the adiabatic $Y$-junction, the optical power transmitted at the output port depends on the phase shift $\Delta\Phi$ experienced by the wave propagating in the biosensing region.

In both the interferometric configurations the output power is affected by the refractive index variation in the sensitive area (of length $L$ in Fig. 4), which ranges between $n_{bio} = 1.33$ and $n_{bio} = 1.4$ [27]. In order to achieve the optimum value of the sensitive area length, which ensures the linearity of the device response, the theoretical output power characteristics for each interferometer have been analyzed.

The theoretical output power, normalized to the input one, as a function of the phase shift $\Delta\Phi$ is given by the following equations [30]:

$$P_{\mathrm{MZI}} = \cos^2\left(\frac{\Delta\Phi_{\mathrm{MZI}}}{2}\right) \tag{3}$$

for the MZI, and

$$P_{\mathrm{MI}} = \sin^2\left(\frac{\Delta\Phi_{\mathrm{MI}}}{2}\right) \tag{4}$$

for the MI.

The phase shift $\Delta\Phi$ between the reference arm and the sensitive one is for the MZI:

$$\Delta\Phi_{\mathrm{MZI}} = \frac{2\pi}{\lambda} L_{\mathrm{MZI}} \Delta n_{\mathit{eff}}, \tag{5}$$

and for the MI:

$$\Delta\Phi_{\mathrm{MI}} = \frac{4\pi}{\lambda} L_{\mathrm{MI}} \Delta n_{\mathit{eff}} \tag{6}$$

where $\Delta n_{\mathit{eff}}$ is the effective refractive index difference between the reference and the sensitive arms, which varies with the biolayer refractive index and, therefore, with the concentration of the biological agent.

The range of variability of $\Delta n_{eff}$ is strictly related to the variation of the biolayer refractive index in the range between $n_{bio} = 1.33$ and $n_{bio} = 1.4$. The phase shifts $\Delta\Phi_{\mathrm{MZI}}$ and $\Delta\Phi_{\mathrm{MI}}$, calculated according to Eqs. (5) and (6), change linearly as a function of the length of the sensitive region therefore, to parity of $\Delta n_{eff}$, the output characteristic of the interferometric biosensors can be tailored by choosing the optimal length of the sensitive region.

Figures 5(a) and 5(b) show the biosensor normalized output powers $P_{\mathrm{MZI}}$ and $P_{\mathrm{MI}}$, respectively, as a function of the phase shifts $\Delta\Phi_{\mathrm{MZI}}$ and $\Delta\Phi_{\mathrm{MI}}$, expressed both in radians and degrees in the case of the channel waveguide structure of Fig. 1(a). Each section of the solid curves corresponds to a different value of the sensitive region lengths, $L_{\mathrm{MZI}}$ and $L_{\mathrm{MI}}$, and is calculated by changing the biolayer refractive index from $n_{bio}$=1.33 to $n_{bio} = 1.4$ for each examined $L_{\mathrm{MZI}}$ and $L_{\mathrm{MI}}$ value. The white area in Fig. 5 delimits the chosen range of linearity of the output characteristic (i.e., deviation from the line tangent at the inflection point less than 3%). In Figs. 5(a) and 5(b), the points corresponding to the refractive index values $n_{bio} = 1.33$ and $n_{bio} = 1.4$ are denoted by the letters A and B, respectively. As expected, from

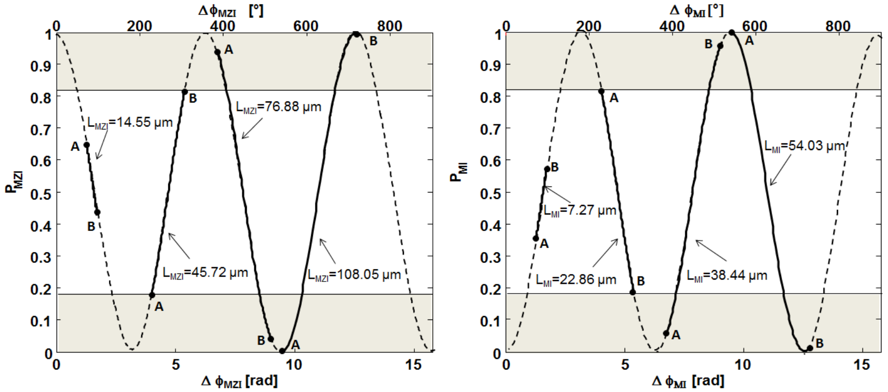

(a) (b)

**Figure 5.** Normalized output power as a function of the phase shift for the channel waveguide and for different values of the length $L$ of the sensitive region in the cases of (a) Mach-Zehnder and (b) Michelson configurations. Letters A and B denote, respectively, the points corresponding to the biolayer refractive index values $n_{bio} = 1.33$ and $n_{bio} = 1.4$.

**Table 3.** Optimal values, $L_{\mathrm{MZI}}$ and $L_{\mathrm{MI}}$, of the sensitive region length for the MZI and the MI configurations, respectively, calculated considering the channel, rib-inverted, and strip waveguides.

| | $L_{\mathrm{MZI}}$ [μm] | $L_{\mathrm{MI}}$ [μm] |
|---|---|---|
| Channel | 45.718 | 22.859 |
| Strip | 57.717 | 28.859 |
| Inverted-rib | 63.000 | 31.865 |

Fig. 5 we can infer that by increasing the sensitive region length the range of variability of the output power widens. In particular, the lengths $L_{\mathrm{MZI}} = 45.72\,\mu\mathrm{m}$ and $L_{\mathrm{MI}} = 22.86\,\mu\mathrm{m}$, for the MZI and MI respectively, are chosen to assure that the output power covers exactly the whole linearity range. In fact, provided the linear behavior, the maximization of the output power range leads to higher values of the sensitivity expressed as:

$$s = \frac{\Delta P}{\Delta n_{bio}} \tag{7}$$

where $\Delta P$ is the maximum variation of the output power (i.e., $\Delta P_{\mathrm{MZI}}$ and $\Delta P_{\mathrm{MI}}$ in the case of MZI and MI configurations, respectively) and $\Delta n_{bio} = 1.44 - 1.3 = 0.07$ is the range of variability of the biolayer refractive index. Table 3 reports the values of the optimal lengths of the sensitive regions, $L_{\mathrm{MZI}}$ and $L_{\mathrm{MI}}$, for the three waveguide configurations shown in Fig. 1, i.e., channel, strip, and inverted-rib waveguides, for both the MZI and MI configurations.

The proposed structures are compatible with standard fabrication techniques such as spin coating for the polymeric layer deposition, photolithographic patterning, etching, etc.. Possible variations of the optical path lengths due to fabrication imperfections, can slightly shift the output characteristic from the optimal behaviour. In particular, we verified that changes of the length of the sensitive region due to fabrication errors $\Delta L = +1\,\mu\mathrm{m}$ and $\Delta L = -1\,\mu\mathrm{m}$ slightly shift the output characteristic out of the almost linear range (denoted by the white area in Fig. 5 corresponding to 3% error with respect to the line tangent) inducing a higher non-linearity error of about 5%. In applications having very stringent requirements on the sensor linearity, such an effect could be compensated by restricting the sensor operation to the dynamic range delimited by the 3% error area.

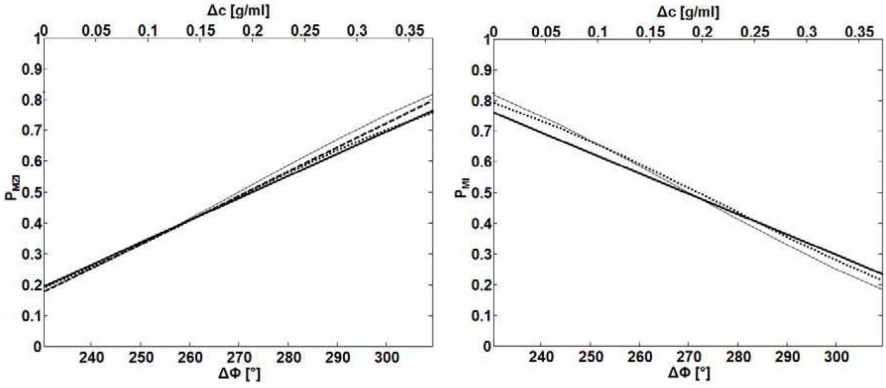

(a) (b)

**Figure 6.** Normalized output power as a function of the phase shift ΔΦ and of the concentration $\Delta c$ for the MZI (a) and MI (b) interferometric biosensors: theoretical characteristic (thin solid curve) and BPM-FFT simulated ones for the channel (dotted curve), the strip (thick solid curve), and the inverted-rib waveguides (dashed curve).

**Table 4.** Optimal values of the geometrical parameters for the MZI configuration, valid for the channel, rib-inverted, and strip waveguides.

| | |
|---|---|
| Input/output waveguide lengths $L_{I/O}$ [µm] | 400 |
| Taper length $L_T$ [µm] | 600 |
| $Y$-junction length $L_Y$ [µm] | 300 |
| Straight arm length $L$ [µm] | 400 |
| $Y$-junction half angle $\theta$ [°] | 0.5 |
| MZI total length [µm] | 3000 |

## 4. INTERFEROMETRIC BIOSENSOR DESIGN

In order to design the two different interferometric configurations, in the cases of the three different waveguides, we have carried out the analysis of the electromagnetic propagation by a home-made computer code based on the Fast Fourier Transform-Beam Propagation Method (FFT-BPM) [31]. Provided the design of the sensitive region length according to the aforesaid considerations, the geometrical parameters of the two biosensor configurations, shown in Fig. 4, have been optimized by means of the FFT-BPM simulations. Since this numerical method allows to take into account the electromagnetic propagation in

**Table 5.** Optimal values of the geometrical parameters for the MI configuration, valid for the channel and strip waveguides.

| | Channel waveguide | Strip waveguide |
|---|---|---|
| Input waveguide width $w_L$ [μm] | 1.5 | 1.5 |
| Adiabatic $Y$-junction length $L_{Ya}$ [μm] | 230 | 230 |
| Taper length $L_T$ [μm] | 50 | 50 |
| Symmetric $Y$-junction length $L_{Ys}$ [μm] | 180 | 180 |
| Adiabatic $Y$-junction half-angle $\theta_1$ [°] | 0.23 | 0.23 |
| Symmetric $Y$-junction half-angle $\theta_2$ [°] | 0.4 | 0.3 |
| MI total length [μm] | 460 | 460 |

the actual waveguide, the occurrence of phenomena such as radiation losses, influence of the optical mode confinement, eventual presence of higher order modes can be considered. In fact, these phenomena can lead to a biosensor output characteristic significantly different from the theoretical one if the actual geometry of the sensor is not optimized.

Table 4 reports the optimal values of the geometrical parameters for the MZI, shown in Fig. 4(a), obtained by the FFT-BPM simulations. These parameters are valid for all the three waveguide configurations considered, whereas the lengths of the sensitive region are those reported in Table 3.

Moreover, Table 5 reports the optimal values of the geometrical parameters for the MI, shown in Fig. 4(b), for the channel and the strip waveguides. The lengths of the sensitive regions are again those reported in Table 3. The data of the inverted-rib structure are not reported because the FFT-BPM simulations have shown that this waveguiding geometry, being characterized by worse mode confinement with respect to the strip and the channel ones, was not efficient for the MI configuration.

The values reported in Tables 4 and 5 for the MZI and MI were optimized by parametric sweep and they were chosen according to the minimization of the error between the output characteristics calculated by the FFT-BPM and the theoretical ones, given by Eqs. (3) and (4).

Figure 6 shows, for both the MZI (Fig. 6(a)) and the MI (Fig. 6(b)), the comparison between the theoretical normalized output power (thin solid curve) and the ones calculated by the BPM-FFT for the different waveguide configurations, i.e., channel (dotted curve), strip (thick solid curve), and inverted-rib (dashed curve). A good agreement is apparent for all the reported interferometric configurations. As already assumed, the inverted-rib waveguide is not included in Fig. 6(b) for the MI configuration owing to its inefficient mode confinement, that gives an output characteristic almost completely different from the theoretical one.

In Fig. 6, the output characteristics of the different biosensors are reported also as a function of the protein concentration, considering that the refractive index increment above that of pure water (i.e., $n_{bio} = 1.33$) with protein concentration $c$ in aqueous phase is linear and it is given by [32]:

$$\frac{\Delta n_{bio}}{\Delta c} \cong 0.188 \left(\frac{\mathrm{g}}{\mathrm{ml}}\right)^{-1}, \tag{8}$$

Therefore, the sensitivity can also be expressed in terms of protein concentration as it follows:

$$s_c = \frac{\Delta P}{\Delta c} = s \cdot 0.188 \left(\frac{\mathrm{g}}{\mathrm{ml}}\right)^{-1}. \tag{9}$$

Table 6 reports the values of the MZI and MI sensitivity, expressed in $(\mathrm{g/ml})^{-1}$ evaluated according to Eqs. (7)–(9) as the ratio between the normalized output power and the protein concentration According to Eq. (8), the sensor dynamic range expressed in terms of protein concentration is equal to $\Delta c = 0.37\,\mathrm{g/ml}$ as given by the range of variability of the biolayer refractive index. The sensitivity and the protein concentration dynamic range depend only on the performance of the sensor itself, irrespective of the overall measurement setup, whereas the measurement setup influences the resolution achievable. As an example, considering an output optical power dynamic range equal to 100 mW the non-normalized sensitivity is equal to 160 mW/(g/ml). Considering an optical power meter, having resolution equal to 1 nW, the minimum measurable value of the protein concentration $c$ in aqueous phase is about 6 ng/ml (i.e., the ratio between the power meter resolution and the non-normalized sensitivity).

**Table 6.** Sensitivity values $s$ and $s_c$ for the various waveguides and the two interferometric configurations.

| | MACH-ZEHNDER | | MICHELSON | |
|---|---|---|---|---|
| | $s$ | $s_c$ [g/ml]$^{-1}$ | $s$ | $s_c$ [g/ml]$^{-1}$ |
| Channel | 8.04 | 1.51 | 8.23 | 1.55 |
| Strip | 8.66 | 1.63 | 8.04 | 1.51 |
| Inverted-rib | 9.03 | 1.70 | – | – |

## 5. CONCLUSIONS

The design of two different kinds of interferometric biosensor, i.e., Mach-Zehnder and Michelson configurations, with three different polymeric waveguides has been carried out. In particular, the design criteria have been pointed out and the theoretical results have been compared with the numerical ones obtained by BPM-FFT. The geometrical parameters of the biosensors have been optimized to maximize the linearity and to achieve high sensitivity values, about equal to $1.6\,(\mathrm{g/ml})^{-1}$. The different biosensor inteferometric configurations are almost equivalent in terms of sensitivity, whereas the Michelson configuration is more compact with respect to the Mach-Zehnder one.

## ACKNOWLEDGMENT

The work has been supported by the Photonic Interconnect Technology for Chip Multiprocessing Architectures ("PHOTONICA") project under the Fondo per gli Investimenti della Ricerca di Base 2008 ("FIRB") program, funded by the Italian government and by the project "Regional laboratory for synthesis and characterization of new organic and nanostructured materials for electronics, photonics, and advanced technologies" funded by the Apulia Region. The research has been conducted in the framework of the European Cooperation in Science and Technology ("COST") Action MP0805.

## REFERENCES

1. Banerjee, A., "Enhanced refractometric optical sensing by using one-dimensional ternary photonic crystals," *Progress In Electromagnetics Research*, Vol. 89, 11–22, 2009.
2. Massaro, A., F. Spano, P. Cazzato, R. Cingolani, and A. Athanassiou, "Innovative optical tactile sensor for robotic system by gold nanocomposite material," *Progress In Electromagnetics Research M*, Vol. 16, 145–158, 2011.
3. Mescia, L., F. Prudenzano, L. Allegretti, G. Calò, M. De Sario, A. D'Orazio, L. Maiorano, T. Palmisano, and V. Petruzzelli, "Design of silica-based photonic crystal fiber for biosensing applications," *Journal of Non-Crystalline Solids*, Vol. 355, 1163–1166, 2009.
4. D'Orazio, A., M. De Sario, C. Giasi, L. Mescia, V. Petruzzelli, and F. Prudenzano, "Design of planar optic sensors for hydrocarbon

detection," *Optical and Quantum Electronics*, Vol. 36, No. 6, 507–526, 2004.

5. Prudenzano, F., L. Mescia, L. A. Allegretti, G. Calò, A. D'Orazio, M. De Sario, T. Palmisano, and V. Petruzzelli, "Design of an optical sensor array for hydrocarbon monitoring," *Optical and Quantum Electronics*, 2009, DOI 10.1007/s11082-009-9322-1.
6. Vincenti, M. A., M. De Sario, V. Petruzzelli, A. D'Orazio, F. Prudenzano, D. De Ceglia, and M. Scalora, "Fabry-Perot microcavity sensor for H2-breath-test analysis," *J. Applied Physics*, Vol. 102, No. 7, 074501, 2007.
7. Stomeo, T., V. Marrocco, V. Petruzzelli, F. Prudenzano, M. Grande, A. Qualtieri, A. Passaseo, and M. De Sario, "Fabrication of force sensors based on two-dimensional photonic crystal technology," *Microelectronic Engineering*, Vol. 84, Nos. 5–8, 1450–1453, 2007.
8. Dostalek, J., J. Ctyroky, J. Homola, E. Brynda, M. Skalsky, P. Nekvindova, J. Spirkova, J. Skvor, and J. Schrofel, "Surface plasmon resonance biosensor based on integrated optical waveguide," *Sens. Actuators B*, Vol. 76, 8–12, 2001.
9. Hopman, W. C. L., P. Pottier, D. Yudistira, J. van Lith, P. V. Lambeck, R. M. De La Rue, A. Driessen, H. J. W. M. Hoekstra, and R. M. de Ridder, "Quasi one-dimensional photonic crystal as a compact building-block for refractometric optical sensors," *IEEE J. Sel. Top. in Quantum Electron.*, Vol. 11, 11–16, 2005.
10. Luo, Z., T. Suyama, X. Xu, and Y. Okuno, "A grating-based plasmon biosensor with high resolution," *Progress In Electromagnetics Research*, Vol. 118, 527–539, 2011.
11. Singh, V. and D. Kumar, "Theoretical modeling of a metal-clad planar waveguide based biosensors for the detection of pseudomonas-like bacteria," *Progress In Electromagnetics Research M*, Vol. 6, 167–184, 2009.
12. Prieto, F., B. Sepulveda, A. Calle, A. Llobera, C. Dominguez, and L. M. Lechug, "Integrated Mach-Zehnder interferometer based on ARROW structures for biosensor applications," *Sens. Actuators B*, Vol. 92, 151–158, 2003.
13. Koerdt, M. and F. Vollertsen, "Fabrication of an integrated optical Mach–Zehnder interferometer based on refractive index modification of polymethylmethacrylate by krypton fluoride excimer laser radiation," *Applied Surface Science*, Vol. 257, 5237–5240, 2011.
14. Lillie, J. J., M. A. Thomas, N.-M. Jokerst, S. E. Ralph, K. A. Dennis, and C. L. Henderson, "Multimode interferometric

sensors on silicon optimized for fully integrated complementary metal-oxide-semiconductor chemical-biological sensor systems," *J. Opt. Soc. Am. B*, Vol. 23, 642–651, 2006.

15. Bruck, R., E. Melnik, P. Muellner, R. Hainberger, and M. Lammerhofer, "Integrated polymer-based Mach-Zehnder interferometer label-free streptavidin biosensor compatible with injection molding," *Biosensors and Bioelectronics*, Vol. 26, 3832–3837, 2011.
16. Xu, Y., Y. Q. Li, Y. Jiang, and C. K. Y. Leung, "Application of $3 \times 3$ coupler based Mach-Zehnder interferometer in delamination patch detection in composite," *NDT&E International*, Vol. 44, 469–476, 2011.
17. Melnik, E., R. Bruck, R. Hainberger, and M. Lämmerhofer, "Multi-step surface functionalization of polyimide based evanescent wave photonic biosensors and application for DNA hybridization by Mach-Zehnder interferometer," *Analytica Chimica Acta*, Vol. 699, 206–215, 2011.
18. Duan, D.-W., Y.-J. Rao, L.-C. Xu, T. Zhu, D. Wu, and J. Yao, "In-fiber Mach-Zehnder interferometer formed by large lateral offset fusion splicing for gases refractive index measurement with high sensitivity," *Sens. and Actuators B*, Vol. 160 1198–1202, 2011.
19. Hong, J., J. S. Choi, G. Han, J. K. Kang, C.-M. Kim, T. S. Kim, and D. S. Yoon, "A Mach-Zehnder interferometer based on silicon oxides for biosensor applications," *Analytica Chimica Acta*, Vol. 573–574, 97–103, 2006.
20. Qi, Z.-M., N. Matsuda, K. Itoh, M. Murabayashi, and C. R. Lavers, "A design for improving the sensitivity of a Mach-Zehnder interferometer to chemical and biological measurands," *Sens. and Actuators B*, Vol. 8, 254–258, 2002.
21. Mosquera, L., J. H. Osório, J. G. Hayashi, and C. M. B. Cordeiro, "Refractometric sensor based on all-fiber coaxial Michelson and Mach-Zehnder interferometers for ethanol detection in fuel," *Journal of Physics: Conference Series*, Vol. 274, 012020, 2011.
22. Meng, H. Y., W. Shen, G. B. Zhang, X. W. Wu, W. Wang, C. Tan, and X. G. Huang, "Michelson interferometer-based fiber-optic sensing of liquid refractive index," *Sens. and Actuators B*, Vol. 160 720–723, 2011.
23. Llobera, A., V. J. Cadarso, M. Darder, C. Domìnguez, and C. Fernàndez-Sànchez, "Full-field photonic biosensors based on tunable bio-doped sol–gel glasses," *Lab Chip*, Vol. 8, 1185–1190, 2008.
24. Stangegaard, M., Z. Wang, J. P. Kutter, M. Dufva, and A. Wolff,

"Whole genome expression profiling using DNA microarray for determining biocompatibility of polymeric surfaces," *Mol. BioSyst*, Vol. 2, 421–428, 2006.

25. Koerdt, M. and F. Vollertsen, "Fabrication of an integrated optical Mach–Zehnder interferometer based on refractive index modification of polymethylmethacrylate by krypton fluoride excimer laser radiation," *Applied Surface Science*, Vol. 257, 5237–5240, 2011.
26. Esinenco, D., S. D. Psoma, M. Kusko, A. Schneider, and R. Muller, "SU-8 Micro-Biosensor based on Mach-Zehnder Interferometer," *Rev. Adv. Mater. Sci*, Vol. 10, 295–299, 2005.
27. Lu, B. J., et al., "Integrated optical Mach-Zehnder biosensor," *J. Light. Tech.*, Vol. 16, No. 4, 583–592, 1998.
28. De Sario, M., A. D'Orazio, and V. Lanave, "Realistic design of a WDM duplexer made from LiNbO3 optical filters," *J. Phys. D*, Vol. 21, s147–s149, 1988.
29. Buus, J., "The effective index method and its application to semiconductor laser," *IEEE J. Quant. Elect.*, Vol. 18, 1083–1089, 1982.
30. Liu, J.-M., *Photonic Devices*, Cambridge University Press, 2005.
31. D'Alessandro, A., F. Campoli, P. Maltese, G. Chessa, A. D'Orazio, and V. Petruzzelli, "Design of an ultrashort directional coupler with an SSFLC coupling layer," *Molecular Crystals and Liquid Crystals*, Vol. 320, 355–364, 1998.
32. DeFeijter, J. A., J. Benjamins, and F. A. Veer, "Ellipsometry as a tool to study the adsorption behavior of synthetic and biopolymers at the air-water interface," *Biopolymers*, Vol. 17, 1759–1772, 1978.